

# Optical pump-probe scanning tunneling microscopy for probing ultrafast dynamics on the nanoscale

S. Yoshida, Y. Terada, M. Yokota, O. Takeuchi, H. Oigawa and H. Shigekawa<sup>a</sup>

Graduate School of Pure and Applied Sciences, University of Tsukuba, Tsukuba 305-8571,  
Japan

Received 18 March 2013 / Received in final form 12 May 2013

Published online 15 July 2013

**Abstract.** The development of a method for exploring the ultrafast transient dynamics in small organized structures with high spatial resolution is expected to be a basis for further advances in current science and technology. Recently, we have developed a new microscopy technique by combining scanning tunneling microscopy (STM) with ultrashort-pulse laser technology, which enables the visualization of ultrafast carrier dynamics even on the single-atomic level. A nonequilibrium carrier distribution is generated using ultrashort laser pulses and its relaxation processes are probed by STM using the optical pump-probe method realized in STM by the pulse-picking technique. In this paper, the fundamentals of the new microscopy technique are overviewed.

## 1 Introduction

The development of current physics and devices has been progressing with the innovation of atomically controlled fabrication technologies. The understanding and control of quantum dynamics, such as the quantum transition and transport in organized small structures, are expected to be key factors in realizing further advances. However, for example, with the miniaturization of functional devices consisting of composite materials, quantum dynamics, which has been analyzed by techniques providing spatially and/or temporally averaged information, does not provide a sufficiently detailed description for the analysis and design of macroscopic functions. Atomic-scale defects, for example, have markedly changed the entire situation: defects, which were once considered as a problem to be avoided, are now actively designed and controlled to realize desired functions. The fluctuation in the distribution of dopant materials governs the characteristic properties of macroscopic functions of materials and devices. Therefore, the evaluation of transient quantum dynamics on the nanoscale is of great importance.

Scanning tunneling microscopy (STM) has been one of the most promising techniques widely used for the analysis of such properties because of its high spatial

<sup>a</sup> e-mail: <http://dora.bk.tsukuba.ac.jp>

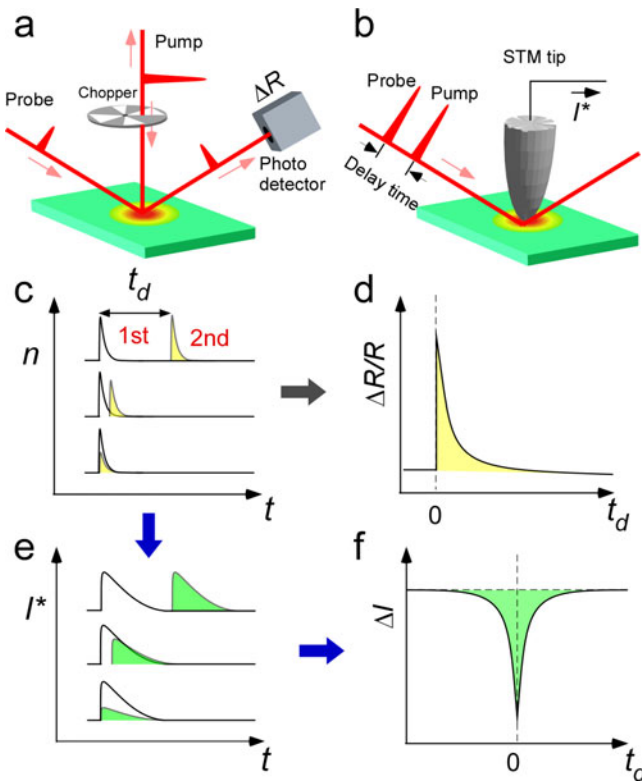


**Fig. 1.** Schematic illustrations of a) OPP method and b) laser-combined STM, and c) to f) their probing mechanisms.

resolution [1–8]. However, since its temporal resolution is low, approximately in the millisecond range, the development of high-time-resolution STM has been an attractive target since its invention. Considerable effort has been devoted to achieving this and various methods and techniques have been developed [9–18].

Recently, time-resolved STM combined with ultrashort-pulse laser technology has been realized [19–29]. A nonequilibrium carrier distribution is generated using ultrashort laser pulses and its relaxation processes are probed by STM using the optical pump-probe (OPP) method realized in STM with the pulse-picking technique. In this paper, the fundamentals of the new microscopy technique and the basic techniques for measurement are overviewed.

## 2 Optical pump-probe STM

### 2.1 Method

Figure 1 shows schematic illustrations of (a) the OPP method and (b) laser-combined STM. In the OPP method (Fig. 1(a)), the sample is illuminated with a sequence of paired laser pulses with a certain delay time  $t_d$ . The first pulses are used to excite the sample (and are therefore called pump pulses) and the second pulses are used as a probe (and are thus called probe pulses) to observe the relaxation of the excited state induced by the first (pump) pulses [30]. As the signal, the reflectivity, for example, of the probe pulses is measured as a function of delay time using a photodetector. Since

the reflectivity of the probe pulse reflects the change in the excited state, such as the production of photocarriers and electronic structures (Fig. 1(c)), if the reflectivity  $R$  of the probe pulse is measured as a function of delay time, the relaxation induced by the pump pulse can be observed through the change in the reflectivity of the probe pulse (Fig. 1(d)). When the carriers excited by the pump pulse remain in the excited state, the excitation by the probe pulse is suppressed, that is, absorption bleaching occurs. In Fig. 1(c), in consideration of absorption bleaching as an example mechanism, the excitation by the probe pulse is drawn smaller than that by the pump pulse. Since the average intensity of the probe pulses is measured as the signal, ultrafast dynamics, which is much faster than the time resolution of the photodetector, can be probed. To probe a weak signal,  $\Delta R < 0.1\%$ , a lock-in detection method is used with chopped light as the reference.

In laser-combined STM, the sample surface beneath the microscope tip is similarly illuminated with a sequence of paired laser pulses with a certain delay time  $t_d$ : however, for the signal, the change in tunneling current  $\Delta I$  is measured as a function of  $t_d$  (Fig. 1(b)). The intensities of the pump and probe pulses are adjusted to be the same. The optical pulses give rise to current pulses in the raw tunneling current  $I^*$  (Fig. 1(e)), reflecting the excitation and relaxation of the sample. When  $t_d$  is sufficiently long compared with the relaxation time of the excited state, the paired optical pulses with the same intensity independently induce two current pulses with the same height in the raw tunneling current. In contrast, when  $t_d$  is short and the probe pulse illuminates a sample excited by the pump pulse, the second current pulse may have a different height, depending on  $t_d$ . The signal  $\Delta I$  therefore also depends on  $t_d$ , because the height difference in the second current pulse changes the temporally averaged value of the tunneling current. Accordingly, the relaxation dynamics of the excited state in the target material, for example, the decay of carrier density after excitation by a pump pulse, can be probed by STM (Fig. 1(f)). In principle, the spatial and temporal resolutions of this microscopy technique are limited by those of the probes used, i.e., the tunneling current (atomic scale) and optical pulse width (femtosecond range).

## 2.2 Probing system

Since the signal, i.e., the photoinduced change in the tunneling current, is weak, we need to use the lock-in detection technique. However, if the laser intensity is modulated for reference, thermal expansion of the STM tip and sample causes a critical problem, because a change in the tip-sample distance of only 1 Å produces a one order change in the tunneling current, making measurement impossible [31]. To realize this microscopy technique, we adopted delay-time modulation, instead of intensity modulation, for the reference in the lock-in detection method, which does not change the intensity of the laser, enabling the measurement without thermal expansion. We call this microscopy technique shaken-pulse-pair-excited STM (SPPX-STM).

Figure 2 shows a schematic of the two laser-combined STM systems we have developed. In the first system, as shown in Fig. 2(a), we mechanically controlled the optical length with mirrors which is the technique ordinarily used in the OPP method, to change the delay time [19, 20]. Although the first signal was successfully obtained with this system, several aspects of the mechanical control had to be improved to achieve further advances. Namely, to measure a weak signal accurately, for example, stable alignment of the laser beam to keep the laser spot accurately focused immediately below the STM tip, high-frequency modulation to reduce the signal-to-noise (SN) ratio of the tunneling current and a wide range of delay times to enable measurement of dynamics consisting of complex components with various time constants were required.

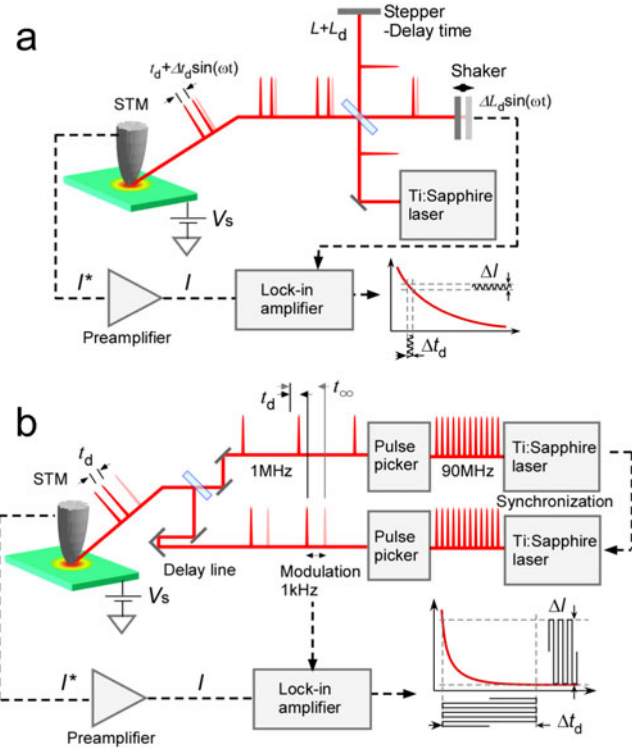


**Fig. 2.** Schematic illustrations of laser-combined STM systems: a) first system, with sine-wave modulation and b) second system with rectangular modulation of delay time.

To satisfy these requirements, in the second system shown in Fig. 2(b), we introduced the discrete modulation of the delay time based on a pulse-picking technique using a Pockels cell, which, for the first time, allowed STM to be used to stably probe carrier dynamics with various time constants in small organized structures over a wide range of time scales [24].

In the second system, pulse trains are generated by two synchronized Ti:sapphire lasers with a 90 MHz repetition rate (11 ns intervals) and a pulse width of 140 fs. The relative timing of the two pulse trains, which provides a delay time that ranges from 0 to 11 ns, is controlled by the synchronizing circuit. Each train is guided to a pulse picker that can selectively transmit one pulse per 90 pulses, resulting in the reduced repetition rate of 1 MHz. The pulse selection enables the production of an additional longer delay time that can be adjusted in multiples of 11 ns. Consequently,  $t_d$  can be adjusted continuously from zero to a large value as needed. Furthermore, the rectangular modulation of  $t_d$  allows the measurement of the absolute value of  $\Delta I(t_d) = I(t_d) - I(\infty)$ , where  $I(\infty)$  is the tunneling current for a delay time sufficiently long for the excited state to be relaxed. The delay time modulated by changing the picking time of the probe pulse between  $t_d^1 (= t_d)$  and  $t_d^2 (= \infty)$ , as shown in Fig. 3(a).

By using rectangular modulation with an amplitude larger than the relaxation time (Fig. 2(b)) instead of sine-wave modulation (Fig. 2(a)) for the lock-in detection, we can measure the absolute value of the signal  $\Delta I(t_d)$  as described above, which increases the signal intensity tenfold compared with the differential value obtained by sine-wave modulation. In addition, since the modulation frequency can be increased from 20 Hz to 1 kHz or more by digital control, the SN ratio can also be improved

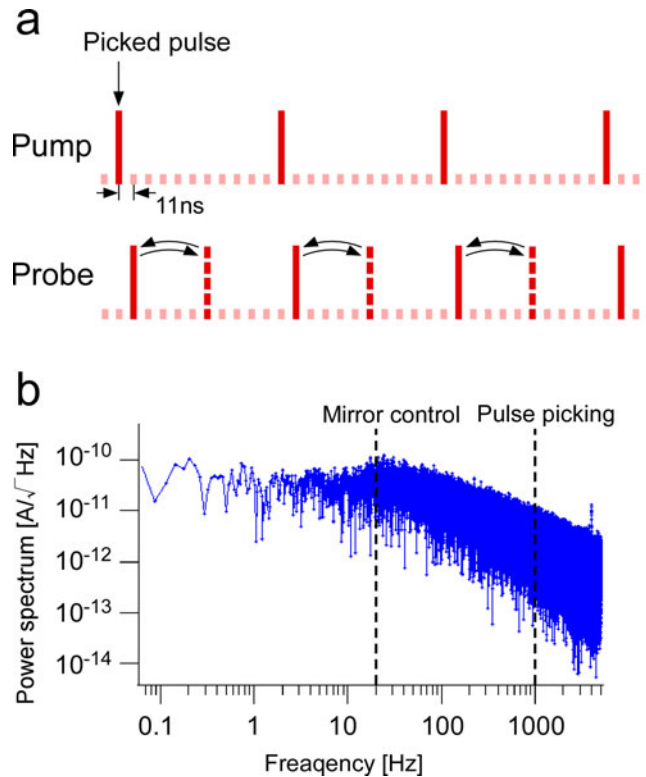


**Fig. 3.** a) Schematic illustration of pulse picking. b) Power spectrum of STM tunneling current.

tenfold as shown by dotted lines in the power spectrum of STM (Fig. 3(b)). Therefore, the SN ratio is improved 100-fold, and therefore, for the same signal level, the measurement time is greatly reduced (by about four orders of magnitude). Accordingly, this method reduces the measurement time and hence enables the spatial mapping of time-resolved signals, which has been desired for a long time [24–26].

Figure 4 shows examples of spectra obtained by SPPX-STM for various samples with a wide range of lifetimes [24]. The upper spectra were obtained by the OPP method, and there is good agreement between both sets of results. With using the new microscopy technique, carrier dynamics can be measured over a wide range of time scales using a single microscope, in principle, from the femtosecond. The carrier dynamics in small organized structures consisting of composite materials can now be evaluated with the spatial resolution of STM.

### 3 Two measurement methods

In scanning tunneling spectroscopy (STS), there are two typical methods of obtaining spectra: (1) One is to acquire a full spectrum  $I(V)$  by measuring the tunneling current  $I$  as a function of bias voltage  $V$  at each point on the sample surface. (2) The other is a type of constant-height-mode measurement, i.e., the tunneling-current map of  $I(V)$  for a certain bias voltage  $V$  is measured over the sample surface by scanning the STM tip, keeping the tip-sample distance constant. By repeating the measurement for various bias voltages, a full series of  $I(V)$  maps, which provides a spectrum  $I(V)$  at

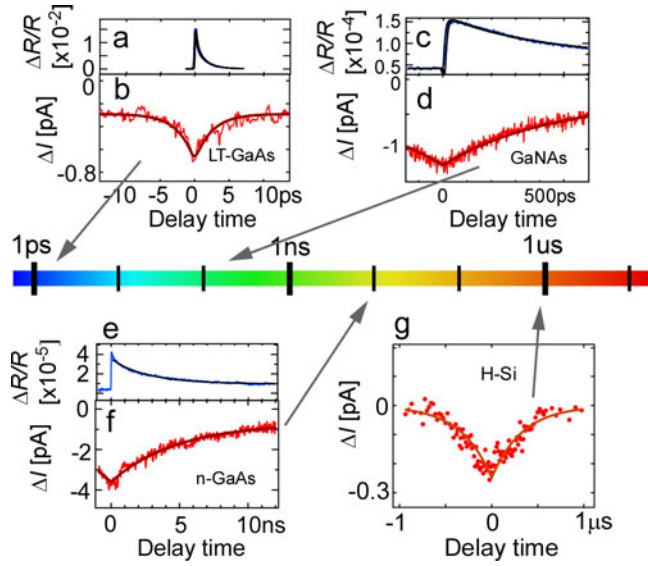


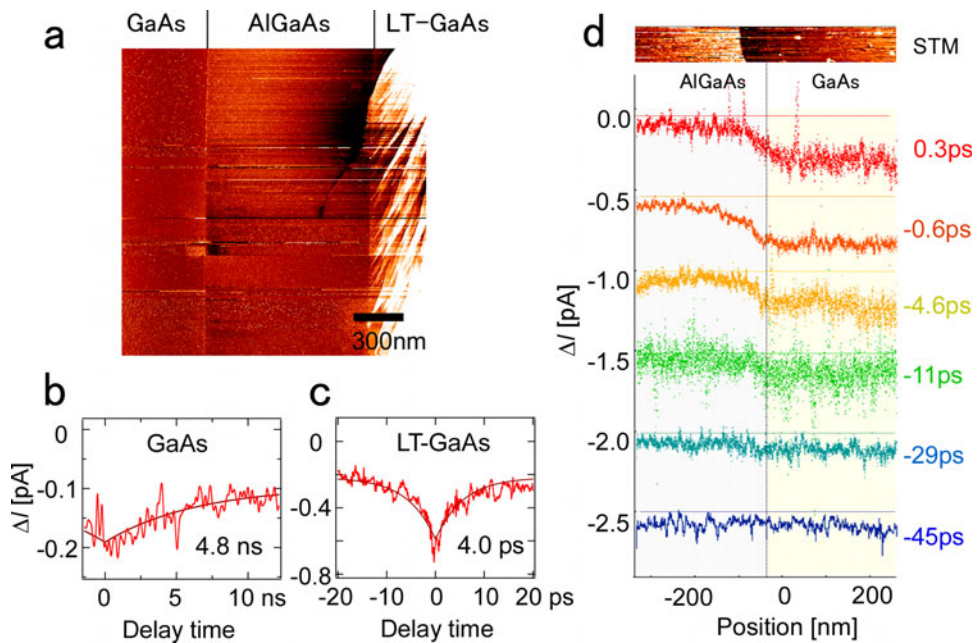
**Fig. 4.** Time-resolved spectra obtained for LT-GaAs, GaNAs, n-GaAs, and H-terminated Si obtained by SPPX-STM. The upper spectra were obtained by the OPP method, and there is good agreement between both sets of results.

each point over the sample surface, can be obtained. These two modes, here referred to as the (1) direct spectrum acquisition (DSA) mode and (2) constant voltage map (CVM) mode, are used depending on the purpose of the experiment.

In time-resolved microscopy, similarly to in STS, there are also two typical methods of obtaining spectra, where the bias voltage  $V$  in the case of STS is replaced by the delay time  $t_d$ . Here, they are referred to as the (1) direct spectrum acquisition (DSA) mode and (2) constant delay-time map (CDM) mode, after those for STS described above.

Figure 5 shows examples of spectra obtained in the two modes [25]. The sample is a semiconductor heterostructure consisting of materials with different lifetimes, GaAs/Al<sub>0.5</sub>Ga<sub>0.5</sub>As/LT-GaAs, where LT-GaAs denotes low-temperature-grown GaAs. A layer of LT-GaAs (1 μm) was grown at 250 °C by molecular beam epitaxy (MBE) on a barrier layer of AlGaAs (1 μm) grown on an undoped GaAs substrate, which was annealed at 700 °C for 60 s in H<sub>2</sub>(5 %)/Ar ambient and contained high-density defects that act as recombination sites for carriers. Thus, the carrier lifetime in LT-GaAs is much shorter than that in GaAs [32]. The lifetimes of photo-carriers in GaAs and LT-GaAs obtained by the OPP method are 4.8 ns and 4.0 ps, respectively. Since the excitation energy (1.55 eV) is lower than the gap energy of AlGaAs (2.3 eV), no signal is expected from AlGaAs.

Measurement can be carried out wherever required because the microscopy technique is STM. Figure 5(a) shows an STM image of a cleaved surface of the sample, where the interfaces between the three layers are clearly recognizable. The typical spectra  $\Delta I(t_d)$  obtained over the areas of GaAs and LT-GaAs in the DSA mode are shown in Figs. 5(b) and 5(c), respectively. As expected, the LT-GaAs region exhibits an ultrafast decay component with a time constant of 4.0 ps, while the GaAs region exhibits decay with a time constant of 4.8 ns. These values are consistent with the recombination lifetimes determined by OPP measurement, 1.5 ps and 2.7 ns for the LT-GaAs and GaAs samples, respectively. The slight difference is considered to originate from the fact that STM probes the local electronic structure, which is an advantage of STM.



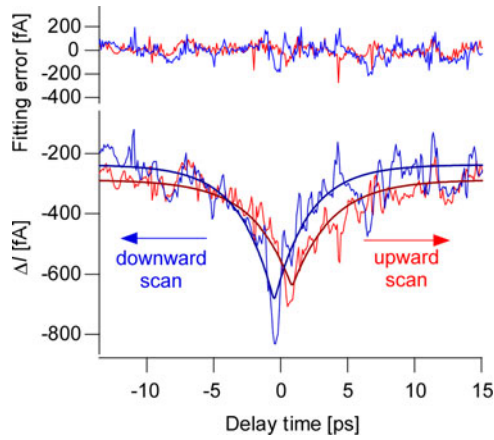
**Fig. 5.** a) STM image of a heterostructure consisting of GaAs, AlGaAs, and LT-GaAs (set point bias voltage  $V_t = 5.5$  V and tunneling current  $I_t = 45$  pA). b) and c) Time-resolved spectra obtained in DSA mode for GaAs and LT-GaAs. d) Time-resolved spectra obtained in CDM mode along the line in a).

Figure 5(d) shows the spectra obtained in the area of STM image on the top by the CDM mode. Here, instead of measuring a full spectrum by changing the delay time (DSA mode), the STM tip was scanned with the delay time fixed at 0.3 ps, 0.6 ps and so forth. Namely, the lines in Fig. 5(d) show the carrier density at each delay time. The carrier density decreases with increasing delay time. When the STM tip is scanned over the entire surface required, two-dimensional (2D) maps of the time-dependent signal can be obtained. The spectrum and its decay constant are obtained from the full series of 2D maps by fitting the change in density at each point.

#### 4 Fitting procedure and time resolution

To obtain a decay constant, we numerically fitted  $\Delta I(t_d)$  spectra using a model function developed as follows. The sample response was assumed to be exponential or double-exponential decay. Then, the sample response was convoluted with an optical pulse profile and the impulse response of low-pass filtering obtained using the lock-in amplifier.

A fitting example is shown in Fig. 6, where the spectra were taken for the LT-GaAs sample shown in Fig. 4. SPPX-STM signals were obtained by repeated upward (red line) and downward (blue line) scans of the delay time. Owing to the finite lock-in time constant, the peak position shifts toward the scan direction of the delay in each spectrum. The best-fit curves are obtained for the two spectra using a model function with the same parameters, as shown by solid lines in Fig. 6. The fitting error (upper part in the figure) is small and comparable to the noise level. The decay constant for the spectrum was found to be 2.4 ps.



**Fig. 6.** Spectra obtained by repeated upward and downward scans of delay time for an LT-GaAs sample and the best-fit curves (lower part). The fitting error is plotted in the upper part.

When the range of delay is much wider than the optical pulse width and the delay-time scan speed is set at a sufficiently low value, the decay constant is not strongly affected by the pulse width and the lock-in time constant, and the fitting of a spectrum using a simple exponential or double exponential function without any convolution is sufficient. In such a case, accurate analysis gives the same decay constant.

The time resolution of the microscopy technique is determined by the optical pulse width, the accuracy of the delay time, and the time constant of the lock-in amplifier. First, the optical pulse width is 140 fs in our setup, which provides a time resolution of  $\sim 200$  fs, determined by the overlap of two optical pulses, that is, the autocorrelation width  $T_0$ . Second, the accuracy of the delay time is mainly determined by that of the mirror position in the optical line and is on the order of 10 fs, which is negligibly small compared with the other factors determining the time resolution. Third, low-pass filtering using the lock-in amplifier also degrades the time resolution. The spectra shown in Fig. 6 were obtained at a lock-in time constant  $T_c$  of 300 ms and a delay-time scan speed  $v$  of 0.54 ps/s, and the corresponding degradation in the time resolution was estimated to be  $vT_c \sim 160$  fs. This value is comparable to  $T_0$ . We carefully adjusted this value to optimize both the SN ratio and the time resolution [19, 20].

On the basis of the above considerations, the time resolution of this microscopy technique is likely to be determined by the first factor, which is the optical pulse width. This is confirmed using the experimental data; as shown in Fig. 6, the fitting error (upper part in the figure) is small and comparable to the noise level. If there are other mechanisms that result in the degradation of time resolution, the signal profile may be further deformed and may not give a good fit. These results indicate that the time resolution of this microscopy technique is limited only by the optical pulse width, which is 140 fs in the present case.

## 5 Time-resolved STM on semiconductor

### 5.1 Mechanism

In laser-combined STM on a semiconductor, a nanoscale metal-insulator-semiconductor (MIS) junction is formed by the STM tip, tunneling gap, and sample.

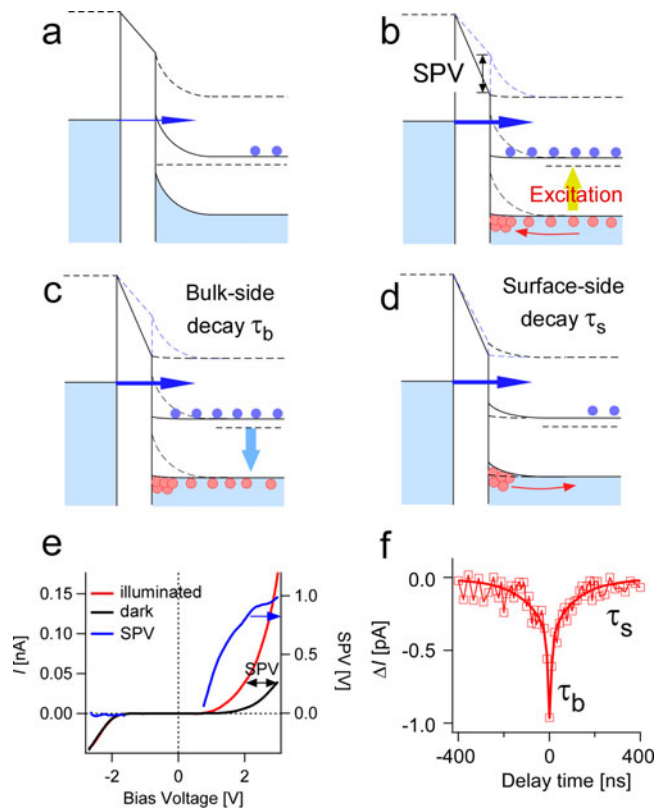


**Fig. 7.** a) Schematic illustrations of metal-insulator-semiconductor (MIS) structures formed by the STM tip, tunneling gap, and sample, and b) to d) their change under photoillumination. e) LM-STS spectrum obtained for GaAs. c) Two components observed in a spectrum: bulk-side decay (decay constant:  $\tau_b$ ) and surface-side decay ( $\tau_s$ ).

When a reverse bias voltage is applied to the junction, tip-induced band bending (TIBB) occurs in the surface region (Fig. 7(a)) [33–36]. When the sample is illuminated, the redistribution of photocarriers reduces the TIBB and surface photovoltage (SPV) is generated (Fig. 7(b)). The magnitudes of TIBB and SPV can be measured by light-modulated-STS [35,36], which provides tunneling current-bias voltage ( $I$ - $V$ ) curves with and without photoillumination simultaneously. From the shift of the two  $I$ - $V$  curves, SPV is obtained for each bias voltage, as shown in Fig. 7(e). When the photoillumination intensity is sufficiently high to flatten the TIBB, the value of SPV corresponds to that of TIBB, i.e., band bending occurs under the dark condition.

The excited state subsequently relaxes to the original state through two processes: (i) decay of the photocarriers on the bulk side (bulk-side decay) via recombination, drift and diffusion (Fig. 7(c)), and (ii) decay of the carriers trapped at the surface (surface-side decay) via recombination and thermionic emission (Fig. 7(d)). Because of the lack of counterpart carriers near the surface, surface-side decay is slower than bulk-side decay. Both decay processes appear in the SPPX-STM signal as follows.

The bulk-side decay is probed, for example, through the mechanism of absorption bleaching, which is a typical mechanism observed in OPP measurement (see 2.1). When the carriers excited by the pump pulse remain in the excited state, the absorption of the probe pulse is suppressed. In such a case, the second current pulse induced in the raw tunnelling current decreases and depends on  $t_d$  (Fig. 1(e)), reflecting the decay of the excited carriers after the pump-pulse excitation (Fig. 1(c)). On the other

hand, the surface-side decay is probed through the mechanism related to SPV. If the probe pulse arrives during the relaxation of SPV induced by the pump pulse, the photocarriers generated by the probe pulse induce SPV again, but the total relaxation time of the SPV depends on the delay time, resulting in change in the total tunneling current,  $\Delta I$ . Accordingly,  $\Delta I(t_d)$  is a measure of the surface-side carrier density at the delay time  $t_d$  as well as the bulk-side carrier density.

Figure 7(f) shows the two components in the spectra, i.e., bulk-side decay ( $\tau_b$ ) and surface-side decay ( $\tau_s$ ). For the case of a p-type semiconductor, photocurrent is directly probed by SPPX-STM [27], which will be discussed in 5.2.

## 5.2 Example of bulk-side decay

We have already seen some examples of results obtained for bulk-side decay (Figs. 4 and 5) for n-type samples, as discussed in detail in 5.1. Here, we give the results obtained for WSe<sub>2</sub>, a p-type semiconductor [27].

Since WSe<sub>2</sub> has an indirect band gap [37], the recombination time of photoexcited carriers is much longer ( $\sim 10 \mu\text{s}$ ), and therefore, the tunneling current is considered to be governed by the balance between the two processes at the surface: the tunneling and diffusion of the photocarriers from the bulk side, which have rates of  $R_t$  and rate  $R_d$ , respectively.

Figure 8(a) shows the laser-intensity dependence of the time-resolved spectra obtained for WSe<sub>2</sub>. When the tip-sample distance is fixed ( $R_t = \text{constant}$ ), the photocarrier density varies with the laser intensity, and the associated change in the diffusion rate  $R_d$  governs the balance. For a low laser intensity ( $R_t \gg R_d$ ), the diffusion rate becomes the limiting factor in the balance, where the tunneling of excess electrons trapped at the surface during photoexcitation is predominantly detected as the signal (fast component, (e), (f), and (g) in Fig. 8(a)). In contrast, for a high laser intensity ( $R_t \ll R_d$ ), the tunneling rate becomes the limiting factor and the diffusion process produces tunneling with a large decay constant (slow component, (a) in Fig. 8(a)). In the intermediate range ( $R_t \sim R_d$ ), the excess electrons trapped at the surface first undergo tunneling. Then, the electrons provided from the bulk side undergo tunneling at a rate of  $R_d$ . As a result, the slow component appears in the time-resolved spectra after the fast component (b), (c), and (d) in Fig. 8(a)).

The decay constants of the fast and slow components are  $\sim 5 \text{ ns}$  and  $\sim 200 \text{ ns}$ , respectively, and that of the slow component is in good agreement with the carrier lifetime obtained by the OPP method,  $\sim 200 \text{ ns}$ , as shown in Fig. 8(b). Figures 8(c) to 8(e) show the schematic illustrations of the band structures to explain the time-evolution processes described above for a negative sample bias voltage with the condition of  $R_t \gg R_d$  ((b), (c) and (d) in Fig. 8(a)). In SPPX-STM, the excess minority carriers transiently trapped at the surface for a few nanoseconds, which produce a transient SPV and cannot be detected by conventional methods, were directly observed and evaluated.

To enable further advances in the application of laser-combined STM, the development of direct techniques for detecting photocurrent in transient dynamics on the nanoscale, such as that shown here, is expected to play an important role in determining the optical characteristics of materials and devices.

## 5.3 Example of surface-side decay

In this section, the analysis of local structures using surface-side decay is discussed. In 5.3.1, the carrier dynamics via in-gap states formed by metal nanoparticles on GaAs is probed by SPPX-STM. A single-atomic-level probe is achieved using the technique

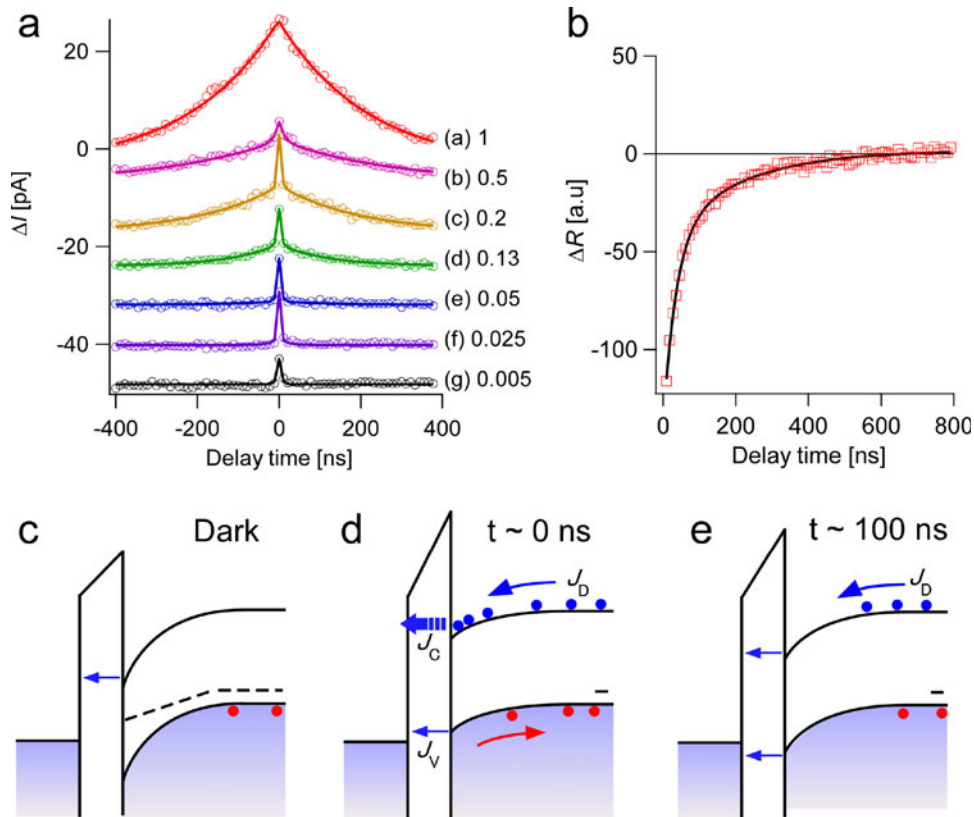


**Fig. 8.** a) Laser-intensity dependence of time-resolved spectra obtained for WSe<sub>2</sub>. The maximum laser intensity was 0.9 mW and the relative intensities were a) 1, b) 0.5, c) 0.25, d) 0.13, e) 0.1, f) 0.05, and g) 0.003. b) Time-resolved spectrum obtained by OPP method. c) to e) Schematic illustrations of the band structures to explain the spectra in a).

of atom tracking. On the other hand, in 5.3.2, the reduction in defect density on a semiconductor surface by (NH<sub>4</sub>)<sub>2</sub>S treatment, which has been used to improve the performance of electronic devices, is examined as an example of the practical application of the microscopy technique [40].

### 5.3.1 Single-atomic-level probing

When some metals are deposited on a semiconductor surface, nanoparticles are formed with gap states, which are considered to enhance the carrier recombination process. We applied SPPX-STM to directly measure the hole-capture rate of (Co, Fe, Mn)/GaAs structures on the atomic scale [24, 29]. Transition metals in semiconductors play essential roles in producing magnetism in dilute magnetic semiconductors (DMSs) [38].

Figure 9(a) shows a schematic of an MIS structure with an in-gap state. Tunneling current, electrons in this case, directly flows from the STM tip into the in-gap state, and the holes trapped at the surface during photoexcitation recombine with the electrons at the in-gap state. There are two limiting factors in this process: tunneling rate ( $W$ ) and hole-capture rate ( $C_P$ ). When the tunneling current is sufficient ( $W \gg C_P$ ), the hole-capture rate becomes the limiting factor of the recombination

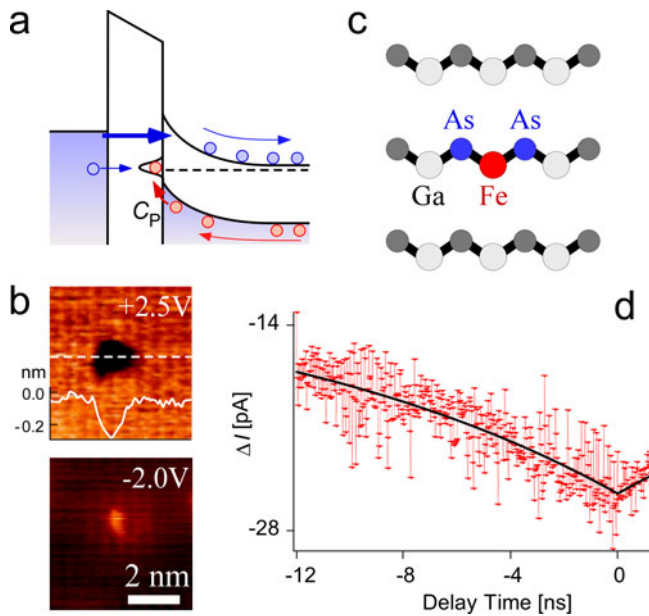


**Fig. 9.** a) Band structure for explaining the carrier dynamics at the in-gap state formed by a metal/GaAs structure. b) Typical STM images of a single-Fe/GaAs structure. c) Schematic model for the single-Fe/GaAs structure. d) Time-resolved spectrum obtained above Fe atom in the single-Fe/GaAs structure.

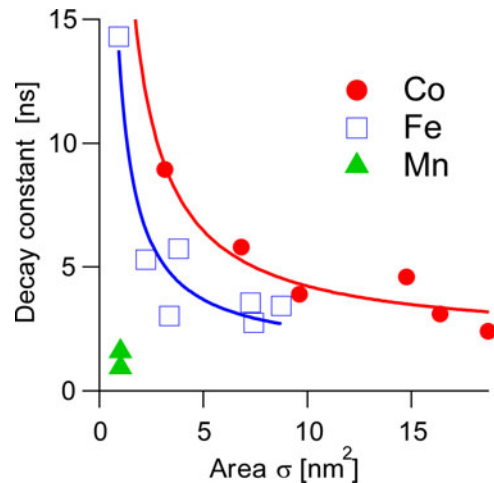


**Fig. 10.** Decay constants obtained by SPPX-STM for (Co, Fe, Mn)/GaAs structures as a function of nanoparticle size. In the results for Fe and Mn, the measurements for the smallest size were carried out on the single-atomic level.

process. In this case, the SPV induced by the pump pulse relaxes with increasing delay time owing to the decay of the trapped holes with the decay constant  $\tau \sim 1/C_P$ . On the other hand, the number of additional holes trapped at the surface by probe-pulse excitation, which further increases the SPV, depends on the SPV remaining after the excitation (delay) time. Therefore, time-resolved STM signal, which probes the change in tunneling current as a function of delay time,  $\Delta I(t_d)$ , gives the hole-capture rate as  $C_P \sim 1/\tau$ .

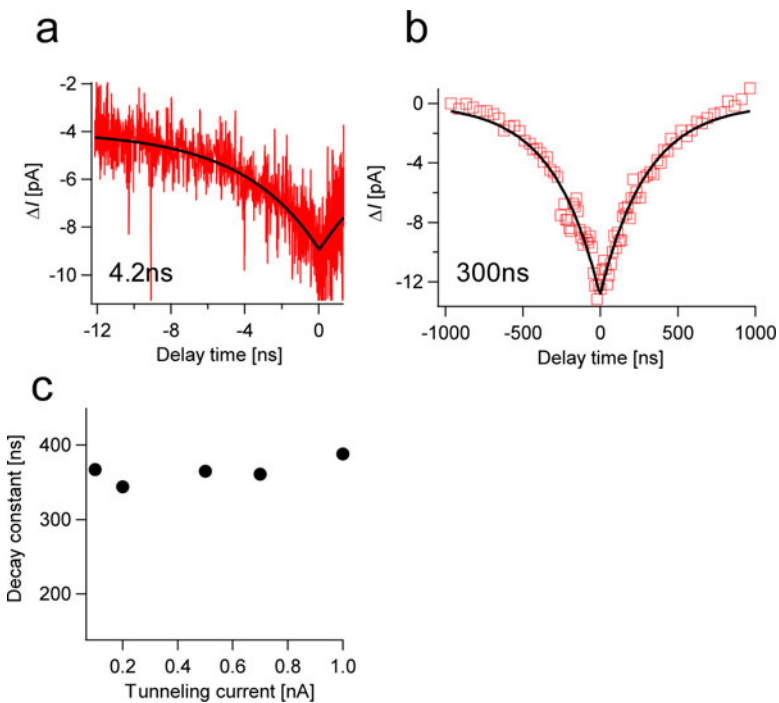


**Fig. 11.** a) Typical time-resolved spectrum obtained in the DAS mode over a) as-etched and b)  $(\text{NH}_4)_2\text{S}$ -treated GaAs(100) surfaces. c) Tunneling-current dependence of carrier decay time obtained for  $(\text{NH}_4)_2\text{S}$ -treated GaAs(100) surface.

Figures 9(b) and 9(c) show typical STM images of a single-Fe/GaAs(110) structure obtained for positive and negative bias voltages and its structural model, respectively. A number of Fe atoms were deposited on a cleaved GaAs(110) surface to prepare the sample. According to previous studies, Fe atoms are considered to occupy the Ga sites on the surface [39]. When the laser intensity is adjusted to satisfy the condition  $W \gg C_P$ , a depression appears at the Fe sites for a positive bias voltage, as shown by the cross section drawn in the STM image, owing to the charging effect of electrons. In such a case, the STM tip position can easily be estimated if the tip is scanned above a single Fe atom during the time-resolved STM measurement. When the STM tip began to probe the edge of the slope of the depression, the tip was moved back to the top of the Fe atom. Figure 9(d) shows a typical spectrum obtained above an Fe atom in the single-Fe/GaAs structure. The decay constant obtained by SPPX-STM was 14.3 ns.

Similar experiments were carried out on Mn/GaAs and Co/GaAs, the results of which are summarized in Fig. 10 along with that for Fe as a function of the nanoparticle size. According to a recent STS measurement [39], the in-gap state of Fe is above that of Co in a bulk, while it is below that of Co at the surface. The in-gap state formed by Mn is the lowest for both cases. The obtained results for the ordering of the levels are in good agreement with the theoretical predictions. Thus, the atomic-scale analysis of the carrier dynamics is now possible by laser-combined STM.

### 5.3.2 $(\text{NH}_4)_2\text{S}$ treatment

High-density defects on semiconductor surfaces deteriorate the performance, for example, of photoelectronic devices. Considerable effort has been devoted to solving this significant problem, and one of the most excellent methods is a surface treatment with

$(\text{NH}_4)_2\text{S}$  solution. According to previous reports,  $(\text{NH}_4)_2\text{S}$  treatment effectively removes the surface oxide and covers the pristine surface with sulfur atoms [40–46]. This method has been widely used to prepare defect-free semiconductor surfaces/interfaces such as for the formation of Schottky junctions and the growth of quantum dots. Here, SPPX-STM was applied to observe the effectiveness of the treatment using surface-side decay, i.e., the effect of the  $(\text{NH}_4)_2\text{S}$  treatment on the minority carrier lifetime at the GaAs(100) surface was investigated [40].

Figure 11 shows the spectra obtained in the DSA mode over (a) as-etched and (b)  $(\text{NH}_4)_2\text{S}$ -treated GaAs(100) surfaces. The decay constant obtained for the  $(\text{NH}_4)_2\text{S}$ -treated surface (361 ns) is two orders longer than that for the as-etched surface (a few ns) and almost the same as that observed for a defect-free GaAs(110) surface ( $\tau_s$  in Fig. 7(e)) [24]. This result is considered to originate from the fact that the number of surface defects of as-etched GaAs induced by oxidation was successfully reduced by the  $(\text{NH}_4)_2\text{S}$  treatment. This is also supported by the measurement of the tunneling-current dependence of carrier decay time; as shown in Fig. 11(c), the decay constant is independent of the tunneling current. Namely, the surface defects, which accelerate the recombination of minority carriers (holes in this case) with the tunneling electrons via the in-gap states, were removed by the  $(\text{NH}_4)_2\text{S}$  treatment. These results are in good agreement with those observed by other techniques such as photoemission spectroscopy [46].

## 6 Conclusion

We have overviewed time-resolved STM, which has been developed by combining STM with ultrashort pulse laser technology, and the fundamentals of the microscopy technique along with experimental results. The OPP method was realized in STM on the basis of delay-time modulation with the pulse-picking technique using a Pockels cell. Using an atom-tacking technique, single-atomic-level measurement has been achieved. On the basis of these techniques, the spatial resolution of STM and the temporal resolution of an ultrashort pulse laser have been realized simultaneously. Direct measurement of the photocurrent by the microscopy technique was also demonstrated.

Support from Japan Society for the Promotion of Science (Grants-in-Aid for Scientific Research) is acknowledged.

## References

1. G. Binning, H. Rohrer, H. Ch. Gerber, E. Weibel, Phys. Rev. Lett. **49**, 57 (1982)
2. R. Wisendanger, *Scanning Probe Microscopy and Spectroscopy* (Cambridge University Press, Cambridge, 1994)
3. M. Berthe, R. Stiufluc, B. Grandidier, D. Deresmes, C. Delerue, D. Stiévenard, Science **319**, 436 (2008)
4. D. Kitchen, A. Richardella, J.-M. Tang, M.E. Flatté, A. Yazdani, Nature **442**, 436 (2006)
5. M.-X. Wang, et al., Science **336**, 52 (2012)
6. A.A. Khajetoorians, B. Chilian, J. Wiebe, S. Schuwalow, F. Lechermann, R. Wiesendanger, Nature **467**, 1084 (2010)
7. T. Komeda, H. Isshiki, J. Liu, Y.-F. Zhang, N. Lorente, K. Katoh, B.K. Breedlove, M. Yamashita, Nat. Commun. **2**, 217 (2011)
8. T. Okuda, T. Eguchi, K. Akiyama, A. Harasawa, T. Kinoshita, Y. Hasegawa, M. Kawamori, Y. Haruyama, S. Matsui, Phys. Rev. Lett. **102**, 105503 (2009)
9. H.J. Mamin, H. Birk, P. Wimmer, D. Rugar, J. Appl. Phys. **75**, 161 (1994)
10. U. Kemiktarak, T. Ndukum, K.C. Schwab, K.L. Ekinci, Nature **450**, 85 (2007)
11. S. Weiss, D.F. Ogletree, D. Botkin, M. Salmeron, D.S. Chemla, Appl. Phys. Lett. **63**, 2567 (1993)
12. G. Nunes Jr, M.R. Freeman, Science **262**, 1029 (1993)

13. I. Moult, M. Herve, Y. Pennec, *Appl. Phys. Lett.* **98**, 233103 (2011)
14. S. Loth, M. Etzkorn, C.P. Lutz, D.M. Eigler, A.J. Heinrich, *Science* **329**, 1628 (2010)
15. R.J. Hamers, David G. Cahill, *Appl. Phys. Lett.* **57**, 2031 (1990)
16. S.W. Wu, W. Ho, *Phys. Rev. B* **82**, 085444 (2010)
17. I. Moult, M. Herve, Y. Pennec, *Appl. Phys. Lett.* **98**, 233013 (2011)
18. C. Saunus, J.R. Bindel, M. Pratzer, M. Morgenstern, *Appl. Phys. Lett.* **102**, 051601 (2013)
19. O. Takeuchi, M. Aoyama, R. Oshima, Y. Okada, H. Oigawa, N. Sano, H. Shigekawa, R. Morita, M. Yamashita, *Appl. Phys. Lett.* **85**, 3268 (2004)
20. M. Yamashita, H. Shigekawa, R. Morita, *Mono-Cycle Photonics and Optical Scanning Tunneling Microscopy-Route to Femtosecond Angstrom Technology* (Springer, Berlin, Heidelberg, 2005)
21. O. Takeuchi, M. Aoyama, H. Shigekawa, *Jpn. J. Appl. Phys.* **44**, 5354 (2005)
22. Y. Terada, S. Yoshida, O. Takeuchi, H. Shigekawa, *J. Phys. Cond. Mat.* **22**, 264008 (2010)
23. H. Shigekawa, S. Yoshida, O. Takeuchi, M. Aoyama, Y. Terada, H. Kondo, H. Oigawa, *Thin Solid Films* **516**, 2348 (2008)
24. Y. Terada, S. Yoshida, O. Takeuchi, H. Shigekawa, *Nature Photonics* **4**, 869 (2010)
25. Y. Terada, S. Yoshida, O. Takeuchi H. Shigekawa, *Adv. Opt. Tech.* **2011**, 510186 (2011)
26. S. Yoshida, Y. Terada, R. Oshima, O. Takeuchi H. Shigekawa, *Nanoscale* **4**, 757 (2012)
27. S. Yoshida, Y. Terada, M. Yokota, O. Takeuchi, Y. Mera, H. Shigekawa, *Appl. Phys. Exp.* **6**, 016601 (2013)
28. H. Shigekawa, O. Takeuchi, Y. Terada, S. Yoshida, *Series: Handbook of Nanophysics, vol. 6, Principles and Methods*, edited by Klaus Sattler (Taylor & Francis, New York, 2010)
29. S. Yoshida, M. Yokota, O. Takeuchi, H. Oigawa, Y. Mera, H. Shigekawa, *Appl. Phys. Exp.* **6**, 032401 (2013)
30. J. Shah, *Ultrafast Spectroscopy of Semiconductors and Semiconductor Nanostructures* (Springer, Berlin, Heidelberg, 1999)
31. S. Grafström, *J. Appl. Phys.* **91**, 1717 (2002)
32. S. Gupta, M.Y. Frankel, J.A. Valdmanis, J.F. Whitaker, G.A. Mourou, F.W. Smith, A.R. Calawa, *Appl. Phys. Lett.* **59**, 3276 (1991)
33. M. McEllistrem, G. Haase, D. Chen, R.J. Hamers, *Phys. Rev. Lett.* **70**, 2471 (1993)
34. R.M. Feenstra, Y. Dong, M.P. Semtsiv, W.T. Masselink, *Nanotechnology* **18**, 044015 (2007)
35. O. Takeuchi, S. Yoshida, H. Shigekawa, *Appl. Phys. Lett.* **84**, 3645 (2004)
36. S. Yoshida, Y. Kanitani, R. Oshima, Y. Okada, O. Takeuchi, H. Shigekawa, *Phys. Rev. Lett.* **98**, 026802 (2007)
37. Ch. Sommerhalter, Th.W. Matthes, J. Boneberg, P. Leiderer, M. Ch. Lux-Steiner, *J. Vac. Sci. Technol. B* **15**, 1876 (1997)
38. H. Ohno, in *Semiconductor Spintronics and Quantum Computation*, edited by D.D. Awschalom, N. Samarth, and D. Loss (Springer, Berlin, 2002)
39. A. Richardella, D. Kitchen, A. Yazdani, *Phys. Rev. B* **80**, 045318 (2009)
40. H. Oigawa, M. Yokota, T. Kishizawa, S. Yoshida, O. Takeuchi, H. Shigekawa, Abstracts 20th International Colloquium on Scanning Probe Microscopy, Okinawa (2012), p. 108
41. H. Oigawa, J.-F. Fan, Y. Nannichi, K. Ando, K. Saiki, A. Koma, *Jpn. J. Appl. Phys.* **28**, L340 (1989)
42. J.J. Gu, A.T. Neal, P.D. Ye, *Appl. Phys. Lett.* **99**, 152113 (2011)
43. S. Tsukamoto, N. Koguchi, *Appl. Phys. Lett.* **65**, 2199 (1994)
44. H. Shigekawa, H. Oigawa, K. Miyake, Y. Aiso, Y. Nannichi, T. Hashizume, T. Sakurai, *Appl. Phys. Lett.* **65**, 607 (1994)
45. H. Shigekawa, H. Hashizume, H. Oigawa, K. Motai, Y. Mera, Y. Nannichi, T. Sakurai, *Appl. Phys. Lett.* **59**, 2986 (1991)
46. H. Sugahara, M. Oshima, H. Oigawa, H. Shigekawa, Y. Nannichi, *J. Appl. Phys.* **69**, 4349 (1991)